

Dynamics of braided coronal loops – I. Onset of magnetic reconnection

A.L. Wilmot-Smith, D.I. Pontin and G. Hornig.

Division of Mathematics, University of Dundee, Dundee, DD1 4HN, UK

March 19, 2010

Abstract

The response of the solar coronal magnetic field to small-scale photospheric boundary motions including the possible formation of current sheets via the Parker scenario is one of open questions of solar physics. Here we address the problem via a numerical simulation. The three-dimensional evolution of a braided magnetic field which is initially close to a force-free state is followed using a resistive MHD code. A long-wavelength instability takes place and leads to the formation of two thin current layers. Magnetic reconnection occurs across the current sheets with three-dimensional features shown, including an elliptic magnetic field structure about the reconnection site, and results in an untwisting of the global field structure.

Keywords: Magnetohydrodynamics (MHD) – plasmas – Sun: corona – Sun: magnetic fields

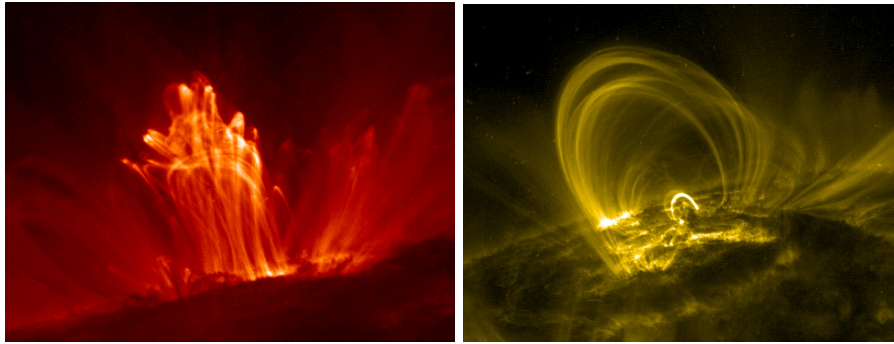


Figure 1: TRACE coronal loops. (*Left*) A large-scale tangled configuration and (*right*) apparently smooth loops.

1 Introduction

Parker’s notion of the ‘topological dissipation’ of coronal magnetic fields (Parker, 1972) continues to generate much debate. Simply put, Parker’s suggestion is that following boundary motions of sufficient complexity the magnetic field of a coronal loop will be unable to ideally relax to a smooth force-free equilibrium and instead tangential discontinuities in the field, corresponding to current sheets, will develop. In general terms the possible outcomes of relaxation are a development of singular current sheets (e.g. Ng & Bhattacharjee, 1998; Janse & Low, 2009), development of thin but non-singular current layers (e.g. Longcope & Strauss, 1994; Galsgaard *et al.* 2003), and a smooth equilibrium with large-scale current features (e.g. van Ballegoijen 1985; Craig & Sneyd, 2005, Wilmot-Smith *et al.* 2009a). It should also be noted that the distinction between the first two cases may be difficult to determine numerically.

In a previous a paper (Wilmot-Smith *et al.* 2009a) we considered the ideal relaxation of a braided magnetic field towards a force-free equilibrium. The magnetic field configuration was based on the pigtail braid and imposed as an initial condition (rather than being built up through boundary motions). This particular braid was chosen since it is the simplest non-trivial braid with no net twist and, accordingly, is the most conservative realistic case to examine. More complex braided fields will, in general, contain components of the pigtail-type. There is ample motivation for modelling loops as having braided components. Photospheric turbulence subjects loop footpoints to a random walk, with motions of the fragments about each other acting to braid (or unbraid) the overlying loop. However, while there is some evidence for the existence of braided loop configurations (see the left-hand image of Figure 1 for example), most coronal loops appear to be close to a potential field (e.g. Figure 1, right-hand image). This may be an effect of the large aspect ratios typical to loops, since a winding of a field line around another field line is almost undetectable when smoothed out over the length of the loop (see also Berger & Asgari-Targhi, 2009). Another reason could be that reconnection is very efficient in maintaining a low degree of topological complexity in loops. The present work is designed in part to test whether this is the case.

In Wilmot-Smith *et al.* (2009a) an ideal Lagrangian relaxation scheme (Craig & Sneyd 1986; Pontin *et al.* 2009) was used to ideally evolve the braided field towards a force-free state. A smooth near force-free equilibrium was attained with large-scale current features i.e. without any tangential discontinuities or even strong current concentrations. (This situation may be compared with Parker (1994) where the same pigtail braid situation is considered as a thought experiment and concluded to inevitably lead to tangential discontinuities. It appears that Parker’s assumption of $\alpha = 0$ in the domain fails; we indeed have $\int \alpha dS = 0$, where S is a cross-sectional surface through the braid, but α varies significantly between field lines).

Although the local current density in the ideal equilibrium is of large-scale, a global quantity, the integrated parallel current, $\int J_{\parallel} dl$, has small scales (here the parallel indicates parallel to the magnetic field and the integral is taken along magnetic field lines). By small scales we mean that $\int J_{\parallel} dl$ varies significantly between neighbouring field lines as the field lines pass through a particular plane, such as the lower boundary. In Wilmot-Smith *et al.* 2009a it was suggested that these small scales in $\int J_{\parallel} dl$ could lead to the development of a resistive instability and so a loss of equilibrium of the field. This mechanism would be distinct to that of Parker’s topological dissipation but have the same consequence.

The consideration that for sufficiently small scales in the integrated parallel current then a force-free magnetic field will be resistively unstable (the instability being dependent, for a given scale in the integrated parallel current, on the value of the resistivity) motivated us to put the end, near force-free, state of the Lagrangian relaxation into a resistive MHD code and test whether or not the state is stable (for various values of resistivity allowed by numerical limitations). It turns out that the braided field as implemented in the resistive code is not stable. This finding, together with the subsequent evolution of the field, allows us to address a number of key questions related to MHD and the behaviour of coronal magnetic fields. The results are described in this series of papers. Here we describe the details relating to the numerical setup of the problem and the early evolution of the system. A subsequent paper addresses the long term evolution of the system.

2 Numerical Scheme and Simulation Setup

2.1 Numerical Scheme

The numerical scheme employed in the simulations that follow is described briefly below (further details may be found in Nordlund & Galsgaard (1997) and at <http://www.astro.ku.dk/~kg>). We solve the

three-dimensional resistive MHD equations in the form

$$\frac{\partial \mathbf{B}}{\partial t} = -\nabla \times \mathbf{E}, \quad (1)$$

$$\mathbf{E} = -(\mathbf{v} \times \mathbf{B}) + \eta \mathbf{J}, \quad (2)$$

$$\mathbf{J} = \nabla \times \mathbf{B}, \quad (3)$$

$$\frac{\partial \rho}{\partial t} = -\nabla \cdot (\rho \mathbf{v}), \quad (4)$$

$$\frac{\partial}{\partial t}(\rho \mathbf{v}) = -\nabla \cdot (\rho \mathbf{v} \mathbf{v} + \underline{\underline{\tau}}) - \nabla P + \mathbf{J} \times \mathbf{B}, \quad (5)$$

$$\frac{\partial e}{\partial t} = -\nabla \cdot (e \mathbf{v}) - P \nabla \cdot \mathbf{v} + Q_{visc} + Q_J, \quad (6)$$

where \mathbf{B} is the magnetic field, \mathbf{E} the electric field, \mathbf{v} the plasma velocity, η the resistivity, \mathbf{J} the electric current, ρ the density, $\underline{\underline{\tau}}$ the viscous stress tensor, P the pressure, e the internal energy, Q_{visc} the viscous dissipation and Q_J the Joule dissipation. An ideal gas is assumed, and hence $P = (\gamma - 1) e = \frac{2}{3} e$. These equations have been non-dimensionalised by setting the magnetic permeability $\mu_0 = 1$, and the gas constant (\mathcal{R}) equal to the mean molecular weight (M). The result is that for a volume in which $|\rho| = |\mathbf{B}| = 1$, time units are such that an Alfvén wave would travel one space unit in one unit of time.

The equations (1-6) are solved on staggered meshes; with respect to a mesh on which ρ and e are defined at the body centre of the cell, \mathbf{B} and P are defined at face centres and \mathbf{E} and \mathbf{J} at edge centres. In this way the required MHD conservation laws are automatically satisfied. Derivatives are calculated using sixth-order finite differences that return a value which is shifted half a grid-point up or down with respect to the input values. When the staggered mesh means that some quantity must be interpolated, data values are calculated using a fifth-order interpolation method at the relevant position. A third-order predictor-corrector method is employed for time-stepping.

In all simulation runs we employ a spatially uniform resistivity model. Viscosity is calculated using a combined second-order and fourth-order method (sometimes termed ‘hyper-viscosity’), which is capable of providing sufficient localised dissipation where necessary to handle the development of numerical instabilities (Nordlund & Galsgaard 1997). The effect is to ‘switch on’ the viscosity where very short length scales develop, while maintaining a minimal amount of viscous dissipation where the velocity field is smooth.

2.2 Creating the Initial Condition

As discussed in Sec. 1, the initial state for the resistive MHD simulations is drawn from the final state of the Lagrangian relaxation experiment of Wilmot-Smith *et al.* 2009a. The quantities previously known from the Lagrangian code (see Craig & Sneyd 1986) are the magnetic field \mathbf{B} and the current \mathbf{J} and in the near force-free relaxed state these are known on a highly distorted mesh. We describe below the process of constructing the field on the rectangular grid required for the resistive MHD simulations.

In order to ensure that the initial magnetic field is divergence-free, we work first with the vector potential \mathbf{A} for \mathbf{B} . In the relaxation scheme, the calculation of \mathbf{A} requires only that we know the initial vector potential before relaxation and the mesh deformation. In terms of the initial mesh \mathbf{X} and the final ‘relaxed mesh’ \mathbf{x} , the i th component of the final vector potential \mathbf{A}^f is given (see Appendix) in terms of the initial vector potential \mathbf{A}^0 by

$$A_i^f = \sum_{j=1}^3 A_j^0 \frac{\partial X_j}{\partial x_i}. \quad (7)$$

To create the input magnetic field for the MHD simulations we then interpolate this vector potential onto a rectangular grid. Since the magnetic field components are face-centred on the staggered grid, the vector potential components are interpolated onto locations corresponding to edge centres of the desired grid. We then obtain the magnetic field by taking the *curl* of \mathbf{A} using the sixth-order finite differences described above, which yields magnetic field components at face-centres as required. An interpolation scheme using biharmonic spline radial basis functions was applied to \mathbf{A} , the particular scheme chosen to maximize the smoothness of the corresponding current density \mathbf{J} , which involves second derivatives of \mathbf{A} . To further improve this smoothness a simple five-point smoothing algorithm was finally applied to \mathbf{A} , before taking the *curl*.

The result of the above is that the initial braided magnetic field for our MHD simulations is divergence-free to accuracies on the order of truncation errors of the sixth-order finite differences (with typical maximum $|\nabla \cdot \mathbf{B}| \sim 10^{-6}$ within the domain). The topology of the magnetic field turns out to be well conserved by the process, another important consideration for the experiment. However, a drawback is that the quality of the force-free approximation is not perfectly maintained; the initial state is further from force-free than the relaxed field of the Lagrangian experiment. Details and implications are discussed in Secs. 3 and 5.

2.3 Initial State

The initial magnetic field is given on a domain of size $[-24, 24]$ in the vertical (z) direction and $[-6, 6]$ in both the horizontal (x, y) directions. Covering this domain we take a uniform mesh of 320^3 cells and employ closed boundary conditions in all three directions. The magnetic field is line-tied, and can be very closely approximated by $\mathbf{B} = [0, 0, 1]$ at the boundaries, i.e. it is directed perpendicular to the z boundaries and parallel to the x and y boundaries. To achieve the perpendicular condition the Lagrangian relaxation experiment was re-run on the larger horizontal domain (now $[-6, 6]^2$ compared with $[-4, 4]^2$ in Wilmot-Smith *et al.* 2009a). The braided field is centered in the middle of the domain and the field is close to uniform in the region external to the braid. Accordingly the results presented here are shown for only the subsection of the full domain in which the important dynamics occur, specifically $[-3, 3]^2 \times [-24, 24]$.

An isosurface of current in the initial state is given the left-hand image of Fig. 2. The current has

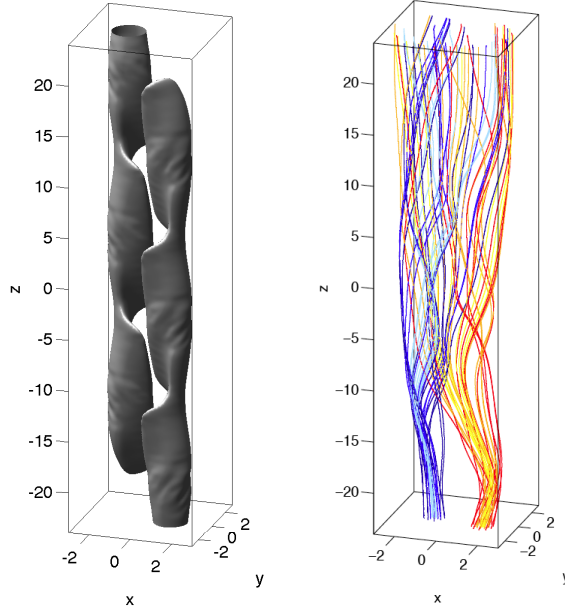


Figure 2: Initial state of the simulation: (*left*) Isosurface of current $|\mathbf{J}|$ at 25% of the domain maximum and (*right*) some particular magnetic field lines illustrating the braided nature of the field.

large-scales (see also the upper-left hand image of Fig. 5 where contours of current in a horizontal cross-section are shown) with two fingers of current extending vertically through the domain. Some sample field lines further illustrating the nature of the field are given in the right-hand image of the same figure. Although non-trivial, the initial state has little magnetic energy in excess of the homogeneous field (0.96% in $[-3, 3]^2 \times [-24, 24]$). The aspect ratio employed in the model is 1:8. Although this is larger than that of many previous simulations it is smaller than a realistic ratio for a coronal loop (1:50, say). In the configuration the poloidal field components are small compared with the toroidal components so that the field lines look almost straight. This level of braiding would be observationally difficult to distinguish from a potential field.

To initialise the simulation the dimensionless plasma density (Sec. 2.1) is set at $\rho = 1$ throughout the domain and the internal energy as $e = 0.1$. The result is a plasma- β at $t = 0$ that lies in the range $\beta \in [0.1, 0.14]$. For the results described in the main section of this paper (Sec. 3) we consider the early evolution of the system (up to $t = 14$) with time measured in units of the Alfvén time. A uniform resistivity of $\eta = 0.001$ has been taken and the effect of changing the resistivity is discussed at various points in the following text.

3 Results

3.1 Basic Properties

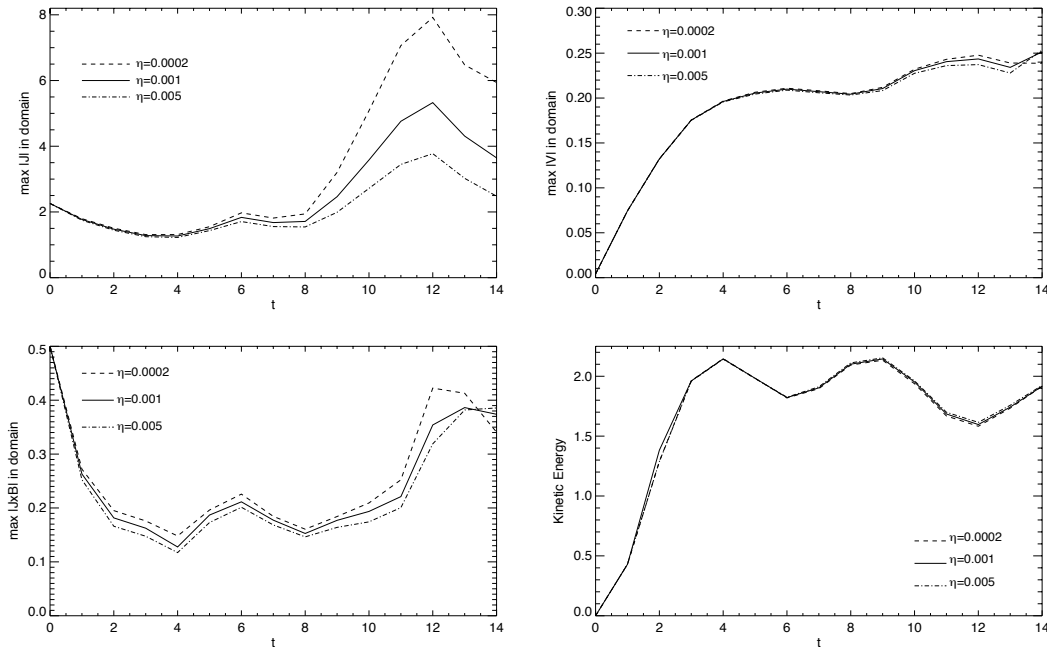


Figure 3: Maximum absolute value of the current (*top left*), velocity (*top right*) and Lorentz force (*bottom left*) and total kinetic energy (*bottom right*) in the domain with time for a sequence of decreasing uniform resistivities as indicated in the figures.

Figure 3 shows the maximum absolute values of the current, velocity and Lorentz force, and the kinetic energy ($\int \frac{1}{2} v^2 dV$) for the time interval ($t \in [0, 14]$) under consideration. The domain taken in all cases is the central section, $[-3, 3]^2 \times [-24, 24]$, of the full box. The variation in quantities is shown for a sequence of uniform resistivities decreasing by over an order of magnitude, specifically $\eta = 0.005, 0.001$ and $\eta = 0.0002$.

The initially high maximum Lorentz force, $|\mathbf{j} \times \mathbf{B}|_{max} = 0.501$ decreases rapidly over the first few time units. Both the high value and the decrease are artifacts of the method used to create the initial state. The interpolation required to transfer the state to the Eulerian grid (as described in Sec. 2.2) results in some noise in the initial magnetic field and current density. Some noise persists even with the application of a smoothing algorithm to the vector potential for the magnetic field and this is particularly noticeable in the Lorentz force rather than the magnetic field and current density alone. Thus whilst the final state of the Lagrangian relaxation experiment had a very small maximum Lorentz force (specifically $|\mathbf{j} \times \mathbf{B}|_{max} \approx 2 \times 10^{-2}$), the initial state here is further from force-free. The decrease over $t \in [0, 2]$ then arises through a smoothing of the noise in the initial state.

Turning now to the remaining quantities shown in Fig. 3, two primary features are found. Firstly a

growth in the kinetic energy and maximum velocity for $t \in [0, 4]$ occurs, and this growth is independent of resistivity, η . For the remaining time considered there is no significant change in kinetic energy. Secondly, a linear growth in the current density occurs for $t \in [8, 12]$. The rate at which the maximum current density increases is higher for lower resistivity, η . At $t = 12$ the maximum current density is achieved; this maximum is higher for lower resistivity but for all three resistivities the growth phase ends at the same time.

The lack of dependence of kinetic energy on resistivity may suggest an ideal instability is present. The subsequent linear growth of current would then be a non-linear consequence of this instability rather than its initial appearance. This growth is clearly dependent on resistivity, being slower for higher values of η . Little is known about the non-linear phase of instabilities and such a dependence may still be consistent with an ideal instability with a non-linear phase damped by η . Strong conclusions are clearly difficult to draw at this stage. An additional consideration is that the implementation of the field on the new grid has resulted in significant Lorentz forces in the initial state. We return to these questions in Section 4 but now proceed to consider the nature of the currents within the domain, now fixing $\eta = 0.001$.

3.2 Formation of Current Layers

Figure 4 shows isosurfaces of current at 50% of the domain maximum ($|\mathbf{J}| = |\mathbf{J}|_{max}/2$) for a sequence of increasing times (for the initial state see Fig. 2). In the early stages ($t \in [0, 4]$) the current diffuses slightly while maintaining its large scales in the perpendicular direction. A symmetric evolution follows and after the phase of current growth two current concentrations are present, centered at $z = 3.4$ and $z = -3.6$. We call these the two ‘initial current layers’.

The formation of these two initial current layers is best illustrated by considering a horizontal cross section through the central plane ($z = 0$). Figure 5 shows contours of the vertical component of current ($|J_z|$) in that plane at $t = 0, 6, 12$. The z -component is taken since it significantly dominates over the two horizontal components, as evident in the shape of the current sheets (Fig. 4). Note that in order to incorporate both sheets the cross-sectional plane chosen, $z = 0$, does not intersect the centre of either current sheet and so the magnitude of current in this plane is somewhat low in comparison to the domain maximum. The collapse of the two oppositely signed large-scale fingers of current present in the initial state into two thin current sheets of correspondingly the same sign is clearly shown. Also evident is the formation of a weaker current envelope around the braided flux, separating it from the uniform background field. Cross-sections of $|J_z|$ in the horizontal planes through the centres of the two current sheets are shown in the final two images of Fig. 7.

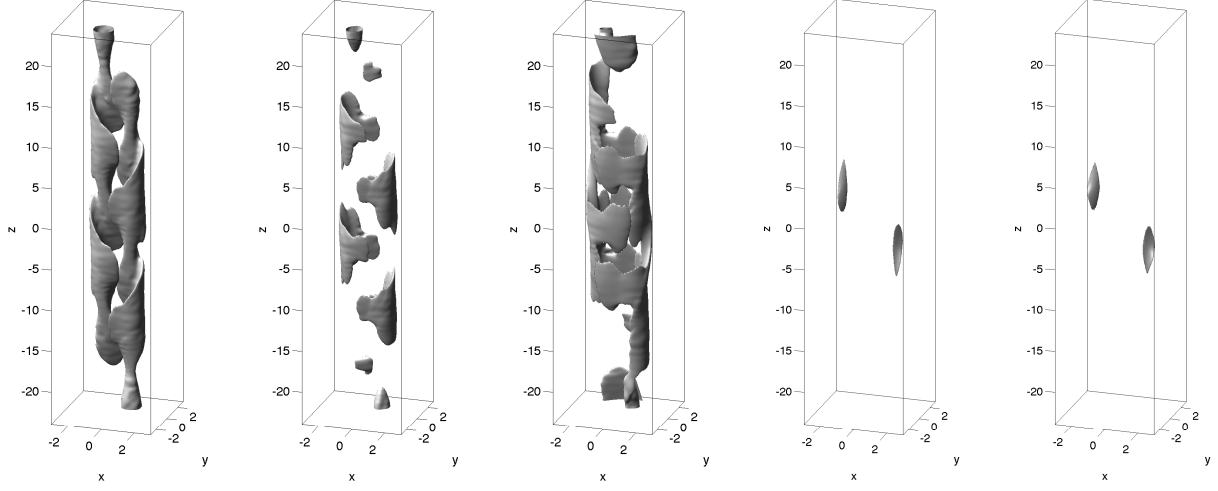


Figure 4: Isosurfaces of current, $|\mathbf{J}|$, at 50% of the domain maximum for a sequence of increasing times (from left to right, $t = 4, 6, 8, 10, 12$) showing the formation of the two initial current layers.

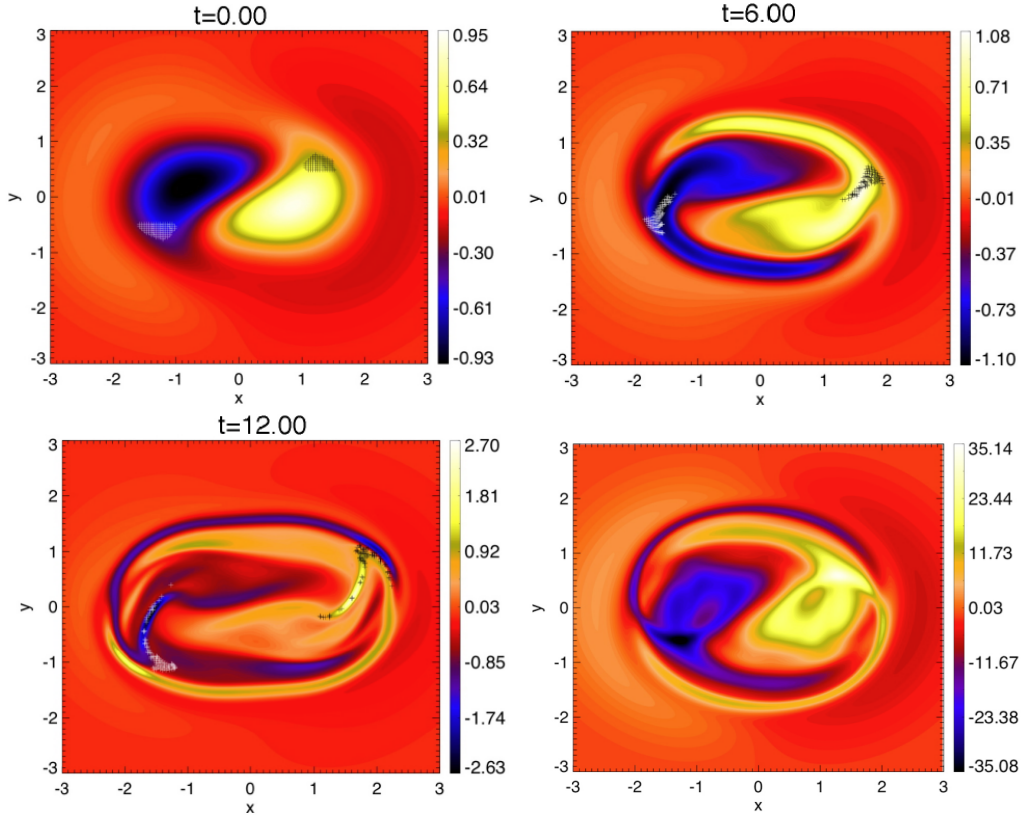


Figure 5: Contours of the vertical component of the current, J_z , in the central plane, $z = 0$, at increasing times, illustrating the formation of the two initial current layers (first three images). The lower right-hand image shows contours of integrated parallel current along field lines in the initial state at the central plane $z = 0$. From this quantity field line tracers for the locations of initially high integrated parallel current have been determined and marked in crosses in the previous frames, as described in the main text.

3.3 Predictors of Current Layers

The field lines along which these two current sheets form turns out to be well predicted by the regions of high integrated parallel current in the initial state. In resistive MHD the integrated parallel current is related to the integrated parallel electric field via the relation $\int J_{\parallel} dl = \eta \int E_{\parallel} dl$ (in the case of a uniform resistivity η , as considered here). The integrated parallel electric field is a key quantity for 3D magnetic reconnection; for a localised reconnection region the maximum value of $\int E_{\parallel} dl$ determines the rate of reconnection.

Shown in the lower right-hand panel of Fig. 5 are contours of the integrated parallel current, $\int J_{\parallel} dl$, in the initial state, $t = 0$, where the path of the integral is taken over magnetic field lines. Again the contour is shown in the central plane ($z = 0$). To obtain this contour map, field lines have been integrated through 160^2 grid of points covering the domain $x, y \in [-3, 3]^2$, $z = 0$. Two peaks in the quantity are present and the structure is quite different to that of the current itself in the initial state. We now identify those field lines in this tracing procedure for which the value of $|\int J_{\parallel} dl|$ is greater than or equal to 75% of the domain maximum, noting the locations where they intersect the lower boundary (where the locations of the field lines are held fixed). For the sequence of times of Fig. 5 we trace field lines starting from those locations on the lower boundary up through the domain and mark with a cross in that same figure their point of intersection with the $z = 0$ plane. Here the difference in colours indicates field lines with positive (black crosses) and negative (white crosses) integrated parallel current, although this distinction is made only to facilitate identification of the locations. It is found that these field lines, traced from the initial locations of high integrated parallel current, are good indicators for the locations of formation of the two current layers. Since the flux on the lower boundary is held fixed these may be identified as the same field lines for as long as the evolution remains ideal. Whilst the evolution will be ideal only during the early stages of the simulation it is clear that the tracers do, nevertheless, provide a useful predictor for the locations of current sheet formation.

Locations of high integrated parallel current are not a commonly used indicator for current sheet formation. Indeed it is quasi-separatrix layers (QSLs), regions where the field-line connectivity varies strongly (Priest & Démoulin, 1995) that are widely thought of as likely sites of current sheet formation. To identify QSLs (as well as their intersections, hyperbolic flux tubes or HFTs) the squashing factor (Titov *et al.* 2002) is used. Usually denoted by Q , the squashing factor is an indicator of field line connectivity and takes on high values in regions where the field line mapping is strongly distorted. Regions of high Q outline QSLs. As discussed in Wilmot-Smith *et al.* (2009b), the braided magnetic field taken as the initial state here contains several QSLs. Contours of the squashing factor, Q , in the central plane ($z = 0$) are shown in Fig. 6 at $t = 0$ (left) and $t = 12$ (right). For the calculation again 160^2 points over the region $x, y \in [-3, 3]^2$ have been used, a number comparable to the grid resolution.

Several regions of high Q are present in both snapshots. The two regions of highest Q in the initial

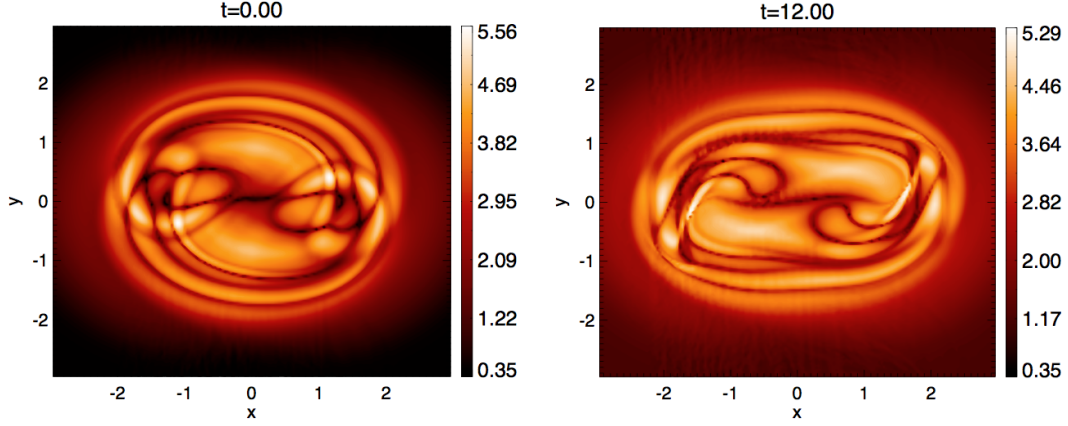


Figure 6: Contours of the squashing factor, specifically $\log_{10}(Q)$, in the central plane, $z = 0$, for (left) the initial state, $t = 0$ and (right) the time $t = 12$.

state are associated with the two initial current layers at the later time, that is, the current sheets have formed along QSLs of the field. At the same time, several other regions of high Q are present (both at $t = 0$ and $t = 12$) that are not associated with any particular current features. For example, in the initial state there are eight distinct regions where $\log_{10}(Q)$ is greater than 85% of its maximum value but only two of these regions correspond to particular current features at $t = 12$. These results suggest that the integrated parallel electric current and the squashing factor could be used in conjunction for predicting current sheet formation more accurately than by using Q alone.

3.4 Plasma Flows and Reconnection

We move now to consider the nature of the plasma flows within the domain. First recall that the low values of the plasma beta (Sec. 2) imply the dynamics will be dominated by the Lorentz force rather than the gas pressure. With both the magnetic field and the current having stronger vertical than horizontal components we have that the Lorentz force is primarily in the horizontal direction and so, similarly, are the plasma flows. The Lorentz force drives a flow with a dipolar structure in the six regions of initially strongest current with direction dependent on the sign of the twist in that region. An illustration of such a flow is shown for the plane $z = 3.4$ (a negative twist region corresponding to one of the sites of current sheet formation) in the first (upper left) image of Fig. 7.

The next four images in that figure show the development of the flow for a sequence of increasing times up to the point of maximum current. In the sequence the length of the arrows indicating flow direction have been normalized to each image. The background contours show the vertical component of current in that plane with the colour scale normalised to the current at $t = 12$ (lower-left-hand image), given by the first colour-bar. The sequence clearly shows the association of the stagnation part of the

dipolar flow with the current intensification. The out-flowing plasma from the location of stagnation sets up a counter-flow to the initial dipolar structure leading to oppositely directed flows on either side of the weak enclosing current sheath. The final image shows plasma flows and current in the plane $z = -3.6$ at $t = 12$. This cross-section is across the second current sheet and shows the naturally expected inversion of the flow direction. The result is that the global flow structure is dominated by rotational components the direction of which varies both vertically along the structure and on either side ($y > 0$, $y < 0$) of the braided field.

As already indicated by Fig. 3, at $t = 12$ the maximum magnitude of the plasma flows ($|\mathbf{V}|_{max} \sim 0.24$) is a significant fraction of the Alfvén speed ($V_A \sim 1.2$). These strongest flows are associated with the global rotation and not with outflows from the two initial current layers (which have an associated $|\mathbf{V}|_{max} \sim 0.15$). However, we do expect magnetic reconnection to be taking place across these current sheets and so proceed to consider the nature of this reconnection. For this we concentrate again on the initial current layer centered at $z = 3.4$ (a similar situation occurs about the other current layer) and focus on the structure of the field and flows in the plane perpendicular to the magnetic field at the location of maximum current magnitude, $|J|$.

In the left-hand image of Fig. 8 we indicate in more detail the nature of the stagnation flow about the current sheet. Superimposed on the background are contours of the out-of plane component of vorticity, i.e. the component of vorticity in the direction of the magnetic field at the location of maximum current. The vorticity shows a quadrupolar configuration around the current sheet.

Perhaps more of a surprise is the structure of the magnetic field in the region. The right-hand image of Fig. 8 shows the components of the magnetic field in the cross-sectional plane under consideration. The magnetic field is shown to have an elliptic configuration about the current sheet, i.e. about the reconnection region. This finding contrasts with the two-dimensional picture of magnetic reconnection under which the process can only occur at a hyperbolic (X-type) null-point of the magnetic field. In three-dimensions a much wider variety of possible reconnection sites exist. Reconnection may be associated with 3D null-points (e.g. Lau & Finn, 1990; Priest & Pontin, 2009), magnetic separators (which connect two null-points, e.g. Longcope & Cowley, 1996; Pontin & Craig, 2006; Haynes *et al.*, 2007), or may occur in the absence of any such topological features (Schindler *et al.*, 1988), the latter sometimes termed ‘non-null reconnection’. In particular, the local magnetic field structure need not be hyperbolic but may be elliptic (Hornig & Priest 2003), as recently found in some 3D numerical simulations of reconnection. For example, Wilmot-Smith & De Moortel (2007) considered reconnection occurring along a quasi-separator and found an elliptic field structure in perpendicular cross-sections. The separator configuration of Parnell *et al.* (2010) showed an elliptic structure along a significant length of the separator under consideration. Parnell *et al.* (2010) also discussed the separator case theoretically, concluding an elliptic configuration would be a generic situation given a sufficiently strong current density along the separator. Our findings demonstrate that an elliptic field configuration may be present about reconnection sites in the non-null

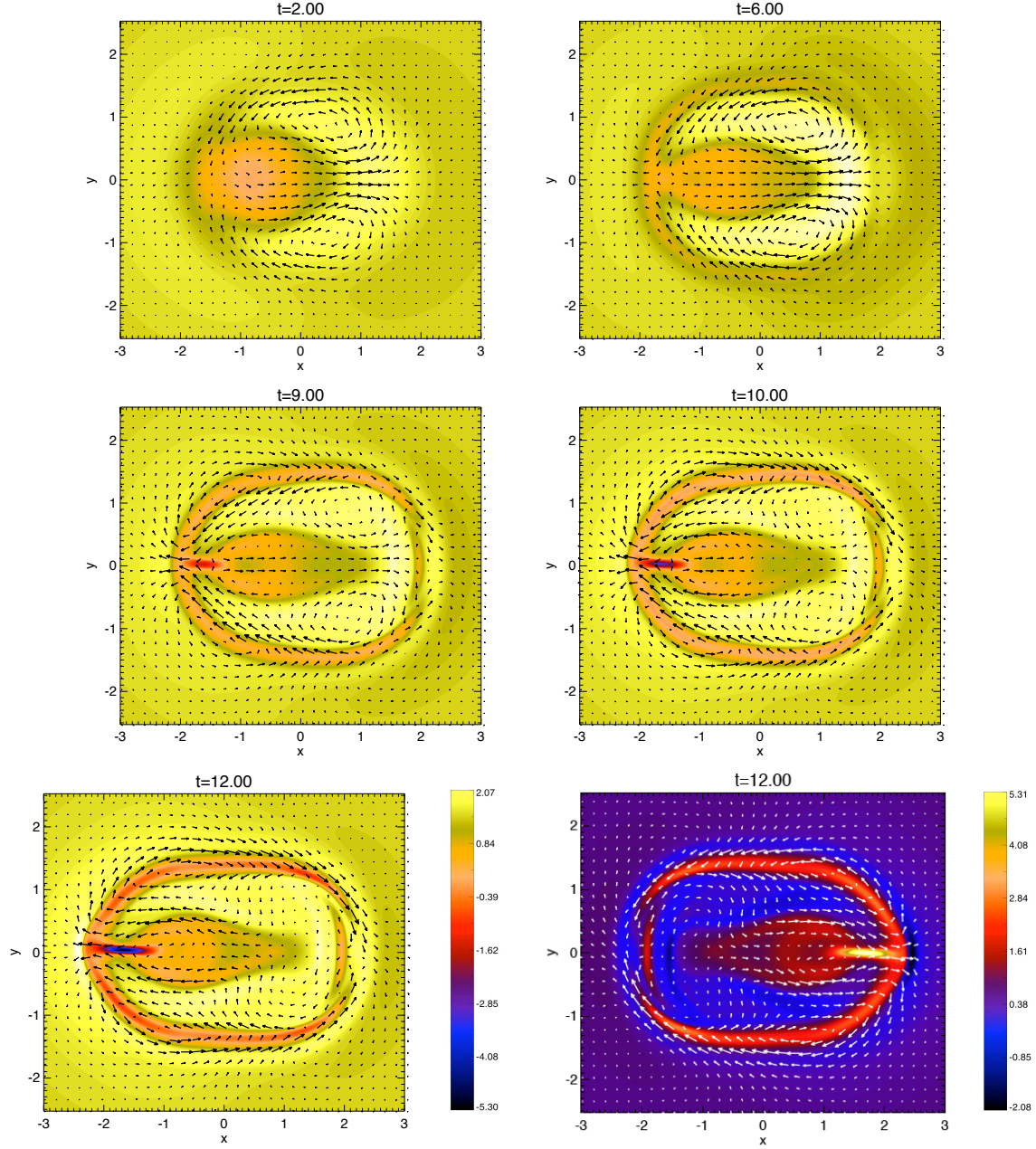


Figure 7: Arrows indicate plasma velocities $[V_x, V_y]$ in horizontal cross-sectional planes, superimposed on the vertical component of current, J_z . The first five images show structures about the upper current sheet (taking the plane $z = 3.4$) while the final image is for the lower current sheet (taking the plane $z = -3.6$). The images are given at various times, as indicated in the figures.

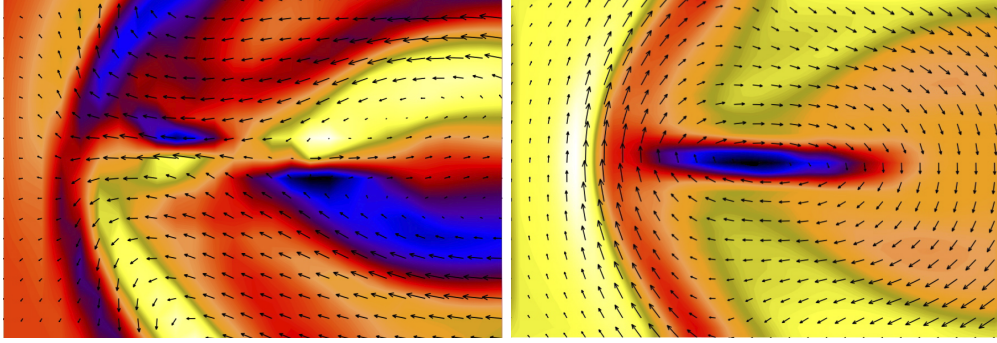


Figure 8: Here various quantities are considered in the plane perpendicular to the magnetic field at the region of maximum (negative) current. (*Left*) Arrows indicate plasma flows in that plane while the coloured contours show the out-of-plane component of vorticity. (*Right*) Arrows indicate magnetic field components in the plane superimposed on contours of the out-of-plane current. The colour table for each is *blue–yellow* for *negative – positive*.

case. Additionally, tracking these field lines back to the initial setup, an elliptic perpendicular field configuration is again found indicating that locally hyperbolic structures are not necessary for current intensification. As previously discussed, the squashing factor (Q) at the two reconnection sites is very high which demonstrates a further point; regions of highest- Q within a domain may have a locally elliptic field configuration.

4 Nature of Instability

Evidently the initial magnetic field configuration is not in a stable equilibrium. Since an exact equilibrium of the ideal relaxation code employed in Wilmot-Smith *et al.* (2009a) is known to be linearly ideally stable, the lack of stability could arise from one of a number of factors:

1. A resistive instability. The relaxed state of Wilmot-Smith *et al.* (2009a) contains small scales in the integrated parallel current. Small enough scales (for a given resistivity) in this quantity are incompatible with a resistive equilibrium.
2. A non-linear ideal instability not previously found in the ideal evolution of Wilmot-Smith *et al.* (2009a) since that evolution only guaranteed linear stability.
3. A lack of equilibrium in the initial state either since:
 - The path to equilibrium of the ideal relaxation is fictitious and an exact equilibrium had not been reached. Numerical difficulties (described in Pontin *et al.* 2009) result in the final state of the ideal relaxation having $|\mathbf{J} \times \mathbf{B}|_{max} \approx 2 \times 10^{-2}$, i.e. is not perfectly force-free. Thus the final state of Wilmot-Smith *et al.* 2009a need not be stable (or, indeed accessible via a real MHD relaxation dynamics).

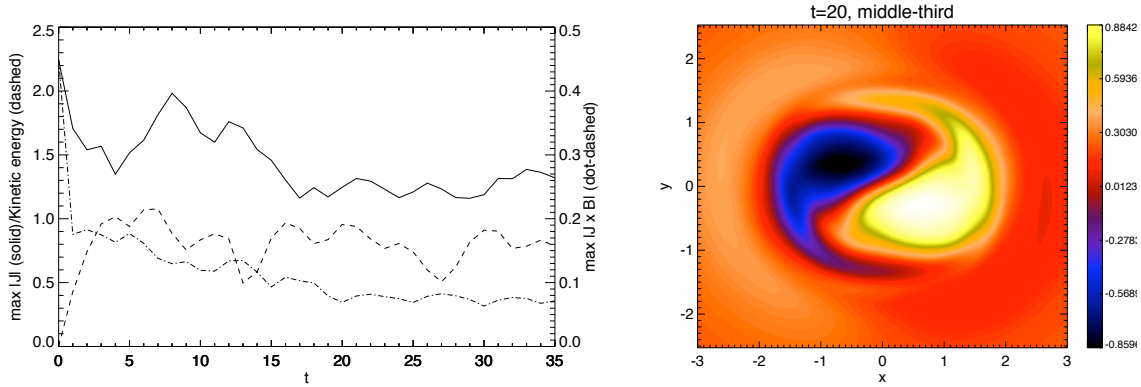


Figure 9: (*Left*) Vertical component of current in the central plane ($z = 0$) at $t = 20$ for the an MHD evolution on only the central section, $z \in [-8.0, 8.0]$ of the full field, as described in the main text. (*Right*) Maximum current $|\mathbf{J}|$ (solid line) and total kinetic energy (dashed line) and maximum Lorentz force (dot-dashed line) over time for the same field.

- The technique used to transfer the initial state between codes has perturbed the magnetic field further from force-free.

At the beginning of Sec. 3 we gave one suggestion, that the formation of the current layers may be due to an ideal instability as evidenced by the lack of dependence of kinetic energy on resistivity (see Fig. 3). Here we seek to determine additional information that may identify the cause of the dynamical evolution. We have noted that the integrated parallel current is a good predictor of the location of the two initial current layers. The integrated parallel current is a global quantity and so the global structure of the field may play a key role. The global structure is also important in, for example, the kink instability where a magnetic field with a set number of turns per unit length becomes unstable as more turns are added by increasing the length of the system. Whilst the kink-instability as it is usually considered applies to a tube with a well-defined single axis a similar kink-like instability, dependent on the total twist of the system, may apply to our braided field.

With these considerations in mind we examine the evolution of only the middle section of the initial state of the braided magnetic field that is, we cut-out the section of the field in the above described experiment that lies in $z \in [-8, 8]$, $x, y \in [-6, 6]$ at $t = 0$. This field is inserted as an initial condition in a new run, now keeping the flux fixed on $z = \pm 8$, the new upper and lower boundaries of the domain. To maintain consistency we use the same resolution in the horizontal direction 320^2 and a similar effective resolution in the vertical direction, 128 cells over $z \in [-8, 8]$.

In the evolution of this new ‘middle-third’ field we find the system adjusts from its initial condition (with zero plasma velocity) to an approximate equilibrium in which the current structure is qualitatively similar to that of the initial state. To illustrate, contours of current in the central plane ($z = 0$) are shown at $t = 20$ in Fig. 9 (right) which may be compared with Fig. 5 (upper left) where the corresponding

contours in the initial state, $t = 0$, are shown. The maximum current in the domain is shown as a solid line in the left-hand image of Fig. 9 (left-hand axis), the kinetic energy integrated over $x, y \in [-3, 3]$, $z \in [-8, 8]$ as a dashed line (left-hand axis) and the maximum Lorentz force within the domain as a dot-dashed line (right-hand axis). As in the evolution of the full field, the Lorentz force in this initial state is high as a result of the transfer between grids and decreases rapidly over the first few time units. However, the Lorentz force subsequently stabilises at a low value as the system readjusts to equilibrium. The result that the middle section of the braid alone is in an equilibrium state suggests that an instability is present in the full braided field (rather than a lack of equilibrium due to numerical artefacts). Furthermore the instability is of a long-wavelength type with the full structure of the braided field being key.

Returning to the evidence of Figure 3, during the time $t \in [8, 12]$ where the instability is clear in the current growth there is only a very slight dependence of the maximum velocity within the domain on resistivity and no increase in kinetic energy. This effect may be due to the confining nature of the strong background field external to the braided field structure which results in a deflection of the outflowing plasma around the boundary of the braided field (see Fig. 7). Prior to $t \approx 8$ no dependence of the flow on resistivity is seen suggesting an ideal dynamics where the system is adjusting to the distance from equilibrium. The current growth in $t \in [8, 12]$ does have a clear separation according to resistivity η . However the increase is linear (rather than exponential) suggesting a dominant non-linear phase and the growth is slower for higher resistivity suggesting the non-linear phase is damped by resistive effects.

5 Conclusions

A previous paper (Wilmot-Smith *et al.* 2009a) considered the ideal relaxation of a braided magnetic field towards a force-free equilibrium. Here we have taken the final state of that relaxation and used it as an initial condition for a full resistive MHD simulation.

The braided field is not in a stable equilibrium; two thin current sheets form after a short time (around a quarter of the time for an Alfvén wave to cross the numerical box in the vertical direction). The linear rate of increase of current density and the maximum strength of the current is found to increase with decreasing resistivity although the evolution of the total kinetic energy in the domain is independent of resolution. We conclude that the instability is possibly an ideal one although the details of how it occurs have not been determined. The wavelength of the instability was tested by considering the MHD evolution of the middle third section of the braid alone and this new field was found to be stable. Hence a long-wavelength dependence is implied.

The initial configuration contains many regions of high squashing factor, Q , corresponding to quasi-separatrix layers. Plasma flow across QSLs is often thought likely to lead to current sheet formation. The two current sheets that form here do align with two of the highest regions of Q although the remaining regions of high Q do not correspond to any particular current features. The locations of the two current

layers are well predicted by the peak values of the integrated parallel current in the initial state. In the central plane this quantity shows two clear peaks and it is at these regions that the two current layers later form.

These two current layers correspond to reconnection sites. Perpendicular to the layers the magnetic field has an elliptic structure, an admissible property of three dimensional reconnection that has only recently been found. The flow about the reconnection sites is of an asymmetric stagnation type, although large-scale rotational flows dominate the global structure; the effect of reconnection is not a strong acceleration of the flow but a more subtle untwisting process leading to the change in magnetic field topology.

The longer-term evolution of the system will be considered in a future paper.

Appendix

Equation (7) can be derived from an evolution for the vector potential of a frozen-in magnetic field:

$$\frac{\partial \mathbf{A}}{\partial t} + \nabla (\mathbf{V} \cdot \mathbf{A}) - \mathbf{V} \times \nabla \times \mathbf{A} = 0. \quad (8)$$

This equation is equivalent to the Lie-derivative for a differential one-form, $\alpha = A_i dx^i$, associated with the vector field \mathbf{A} (Hornig, 1997). Hence (8) can be written as

$$\frac{\partial \alpha}{\partial t} + L_{\mathbf{v}} \alpha = 0, \quad (9)$$

and we can express $\alpha(t=0) = F^* \alpha(t)$ (Abraham *et al.* 1988), or more conveniently $\alpha(t) = (F^{-1})^* \alpha(t=0)$, where $F : X \rightarrow x$ maps the initial to the final coordinates and the star indicates the pull-back operation. This last equation written in components of the vector potential is (7).

Acknowledgements

The authors would like to thank Nasser Al-Salti for helpful suggestions and Klaus Galsgaard for the use of his code. A.W.S. and G.H. acknowledge financial support from the UK's STFC. The simulations described were carried out on the STFC and SFC (SRIF) funded linux clusters of the UKMHD consortium at the University of St Andrews.

The Transition Region and Coronal Explorer, TRACE, is a mission of the Stanford-Lockheed Institute for Space Research (a joint program of the Lockheed-Martin Advanced Technology Centre's Solar and Astrophysics Laboratory and Stanford's Solar Observatories Group), and part of the NASA Small Explorer program.

References

- Abraham, R., Marsden, J.E., Ratiu, T. 1988, *Manifolds Tensor Analysis and Applications*, Applied Mathematical Sciences 75, 370, Springer-Verlag, New York.
- Berger, M.A., Asgari-Targhi, M., 2009, *ApJ*, 705 347-355.
- Craig, I. J. D., Sneyd, A. D. 1986, *ApJ*, 311 451-459.
- Craig, I. J. D., Sneyd, A. D. 2005 *Sol. Phys.*, 232 41-62.
- Galsgaard, K., Titov, V.S., Neukirch, T. 2003, *ApJ*, 595 505.
- Haynes, A.L., Parnell, C.E., Galsgaard, K., Priest, E.R. 2007, *Proc. Roy. Soc. A*, 463 1097-1115.
- Hornig, G. 1997, *Phys. Plasmas* 4, 646-656.
- Hornig, G., Priest, E.R. 2003, *Phys. Plasmas*, 10, 2712-2721.
- Janse, Å. M., Low, B.C. 2009, *ApJ*, 690 1089-1104.
- Lau, Y-T., Finn, J.M. 1990, *ApJ*, 350 672-691.
- Longcope, D.W, Cowley, S.C. 1996, *Phys. Plasmas*, 3 (8) 2885-2897.
- Longcope, D., Strauss, H.R. 1994, *ApJ*, 437, 851-859.
- Ng, C.S., Bhattacharjee, A. 1998, *Phys. Plasmas*, 5, 4028-4040
- Nordlund, A., Galsgaard, K. 1997, A 3D MHD code for parallel computers. Technical report, Astronomical Observatory, Copenhagen University.
- Parker, E.N. *Spontaneous Current Sheets in Magnetic Fields With Applications to Stellar X-Rays*. 1994, Oxford University Press, Inc., New York (pp. 23-24).
- Parnell, C.E., Haynes, A.L., Galsgaard, K. 2010, *JGR*, 115 A02102.
- Pontin, D.I., Craig, I.J.D. 2006, *ApJ*, 642 568-578.
- Pontin, D.I., Hornig, G., Wilmot-Smith, A.L., Craig, I.J.D. 2009, *ApJ*, 700 (2) 1449-1455.
- Priest, E.R., Demoulin, P. 1995, *JGR*, 100 (A12) 23443-23464.
- Priest, E.R., Pontin, D.I. 2009, *Phys. Plasmas*, 16 122101.
- Schindler, K., Hesse, M., Birn, J. 1988, *JGR*, 93 5547-5557.
- Titov, V.S., Hornig, G., Démoulin, P. 2002, *JGR*, (A8) SSH 3-1 1164.
- van Ballegoijen, A.A. 1985, *ApJ*, 298, 421.
- Wilmot-Smith, A.L., De Moortel, I. 2007, *A&A*, 473 615-623.
- Wilmot-Smith, A.L., Hornig, G., Pontin, D. I. 2009a, *ApJ*, 696 1339-1347.
- Wilmot-Smith, A.L., Hornig, G., Pontin, D.I. 2009, *ApJ*, 704 (2) 1288-1295.